buildings

Article

Thermoelastic Behaviors of Temperature-Dependent Multilayer Arches under Thermomechanical Loadings

Zhong Zhang [1], Wenjie Zhao [1], Ying Sun [1,*], Zhenyuan Gu [1], Wangping Qian [1,2] and Hai Gong [3]

1 School of Transportation and Civil Engineering, Nantong University, Nantong 226019, China
2 School of Civil Engineering, Southwest Jiaotong University, Chengdu 610031, China
3 Nantong Prefabricated Building and Intelligent Structure Research Institute, Nantong 226014, China
* Correspondence: ying.sun1993@ntu.edu.cn

Abstract: This work presents analytical solutions for thermoelastic behaviors of multilayer arches with temperature-dependent (TD) thermomechanical properties under thermomechanical loadings. The temperature is varied across the thickness of the arch. Firstly, an arched-slice model is developed, which divides every layer of the arch into numerous hypothetical arched slices with uniform thermomechanical properties. Based on the model, the nonlinear heat conduction equations across the thickness of the arch are solved using the iteration approach, and then the thermoelastic equations obtained from the two-dimensional thermoelasticity theory are solved using the state-space approach and transfer-matrix approach. The present solutions are compared with those obtained using the finite element method and the Euler–Bernoulli theory (EBT). It is found that the error of the EBT increases when the angle of the arch increases or the length-to-thickness ratio decreases. Finally, numerical examples are conducted to analyze the effects of surface temperature and TD thermomechanical properties on the temperature, displacement, and stress distributions of a sandwich arch. The results show that the temperature dependency of thermomechanical properties is a key parameter in predicting the thermoelastic behaviors of the arch in a high-temperature environment.

Keywords: multilayer arch; temperature-dependent thermomechanical properties; arched-slice model; heat conduction; thermoelasticity

Citation: Zhang, Z.; Zhao, W.; Sun, Y.; Gu, Z.; Qian, W.; Gong, H. Thermoelastic Behaviors of Temperature-Dependent Multilayer Arches under Thermomechanical Loadings. *Buildings* **2023**, *13*, 2607. https://doi.org/10.3390/buildings13102607

Academic Editor: Binsheng (Ben) Zhang

Received: 27 September 2023
Revised: 14 October 2023
Accepted: 15 October 2023
Published: 16 October 2023

1. Introduction

Multilayer arches have been widely applied in various engineering structures, such as bridges [1–3] and storage tanks [4,5]. The thermomechanical analysis of the multilayer arches has attracted considerable interest, given that the structures may work in severe environments. For example, the multilayer thermal protection system of space vehicles will suffer aerodynamic heating during hypersonic flying, which makes the thermomechanical analysis important for the design [6]. In addition to inducing thermal stresses, the temperature change in the arches also changes the thermomechanical properties [7,8]. These effects could weaken the load-carrying capacity of the arches, and even cause structural failure. Such a problem needs a thorough study.

Several theories [9,10] for the mechanical analysis of arches have been reported, which are commonly based on the straight beam theories [11–14]. Among these theories, the most basic and popular one is the Euler–Bernoulli theory (EBT), with many successful applications [15–18]. Based on the EBT and state-space approach, the thermal vibration of cross-ply laminated arches was studied by Khdeir [19]. According to the EBT and using Green's function method, Rezaiee-Pajand et al. [20] studied the deformations of arches under thermomechanical loadings. The results showed that the in-plane and out-of-plane displacements can be induced through the lateral temperature distribution. Vargas et al. [21] proposed a method for the static analysis of cross-ply laminated arches under thermomechanical loadings. The EBT was applied to obtain the in-plane stress distributions, while the Airy stress function was applied to obtain the out-of-plane ones. According to the EBT and von Kármán hypothesis, Keibolahi et al. [16] studied the nonlinear vibration of a shallow arch under rapid heating. The Ritz method was applied to discretize the motion equation, and the Newton–Raphson method was applied to obtain the solution.

As a result of the neglect of shear deformation effects, the EBT is only suitable for the analysis of thin arches, but has considerable errors for the analysis of thick arches. Thus, diverse refined theories have been proposed, such as the first-order theory [22–24] and higher-order theories [25–28]. Additionally, the exact thermoelasticity theory [29,30] can also be used to solve the arch problems. Using the thermoelasticity theory, Qian et al. [31] studied the static behavior of laminated arches under thermal loading. The exact thermoelastic solutions were presented by using the Fourier series expansion method.

The above studies were carried out based on the hypothesis of temperature-independent (TI) thermomechanical properties. The hypothesis may be tenable when the arch is under a limited temperature range. However, temperature dependency of thermomechanical properties must be included for a wide temperature range, otherwise considerable errors will arise [32–35]. Based on the EBT, the thermal bending, buckling, and vibration behaviors of temperature-dependent (TD) functionally graded (FG) arches were studied [36–40]. According to the first-order theory, Javani et al. [41] studied the thermally induced vibration of FG shallow arches considering the TD thermomechanical properties. The generalized differential quadrature method was applied to solve the transient heat conduction equation and the motion equation. Using the third-order arch theory and two-step perturbation technique, Babaei et al. [42,43] performed the thermal bending and vibration analysis for TD FG shallow arches. The results indicated that the mechanical performance of the arch was greatly affected by the temperature dependency of thermomechanical properties. Based on a refined tube theory proposed by Zhang and Fu [44], the nonlinear bending behavior of TD shallow curved tubes was studied using the two-step perturbation technique [45,46].

The literature report indicates the lack of analytical solutions for multilayer arches considering TD thermomechanical properties. Motivated by this fact, we propose an arched-slice model to study the thermoelastic behaviors of TD multilayer arches under thermomechanical loadings. Asymptotic analytical solutions of temperature, displacements, and stresses are obtained, and the effects of material and load parameters on the thermoelastic behaviors are discussed.

2. Problem Statement and Arched-Slice Model

A simply supported multilayer circular arch is shown in Figure 1. In the initial stress-free state, the arch is under a uniform temperature. We consider the arch is heated from the inside and outside surfaces and subjected to a radial load $Q(\varphi)$ on the outside surface. The thermomechanical properties of every layer are TD.

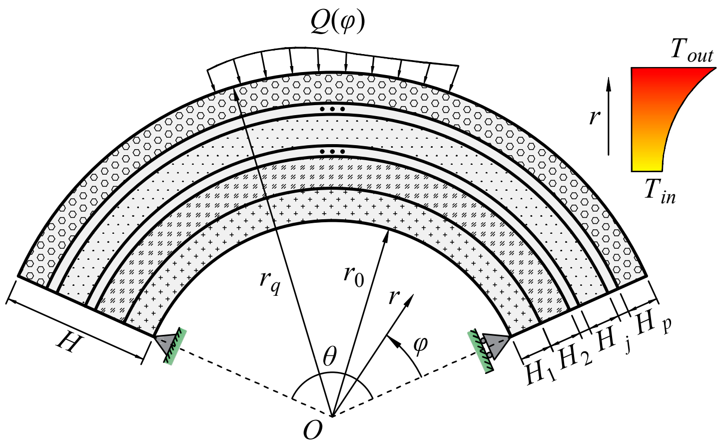

Figure 1. A simply supported multilayer circular arch under thermomechanical loadings.

2.1. Basic Assumptions

The study on the multilayer arch is based on the following assumptions:

i. The inside and outside surface temperatures are uniformly distributed on the surfaces and the two lateral surfaces are adiabatic;
ii. Each layer is made of a homogenous isotropic material with uniform thickness;
iii. Each layer is perfectly bonded with the adjacent layer;
iv. The analysis is within the framework of linear elasticity and small strains.

2.2. Arched-Slice Model

Based on the first assumption, the temperature only varies across the thickness of the arch, hence the thermomechanical properties are also r-dependent. For such a problem, it is impractical to exactly solve the heat conduction equations and thermoelasticity equations due to their r-dependent coefficients. To facilitate asymptotic solutions, we propose an arched-slice model as shown in Figure 2. In this model, every layer is divided into several hypothetical arched slices. When every slice is sufficiently thin, the r-dependent coefficients can be approximated as constant ones by letting $r = \bar{r}_i$ (see Figure 3).

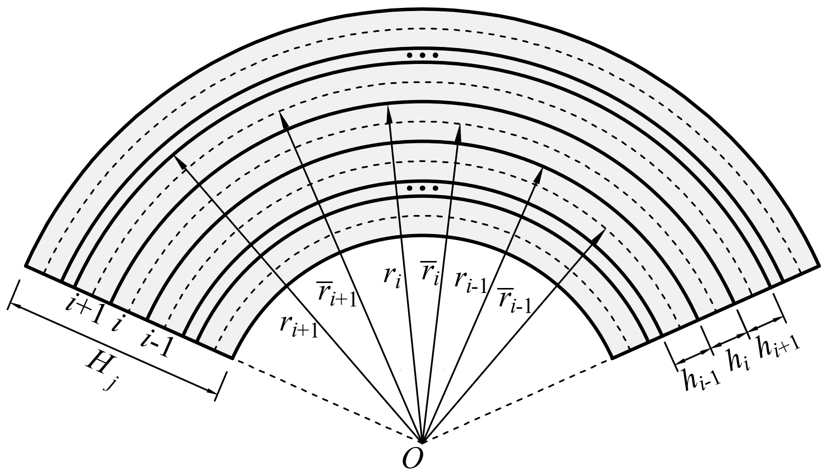

Figure 2. Hypothetical arched slices in a layer.

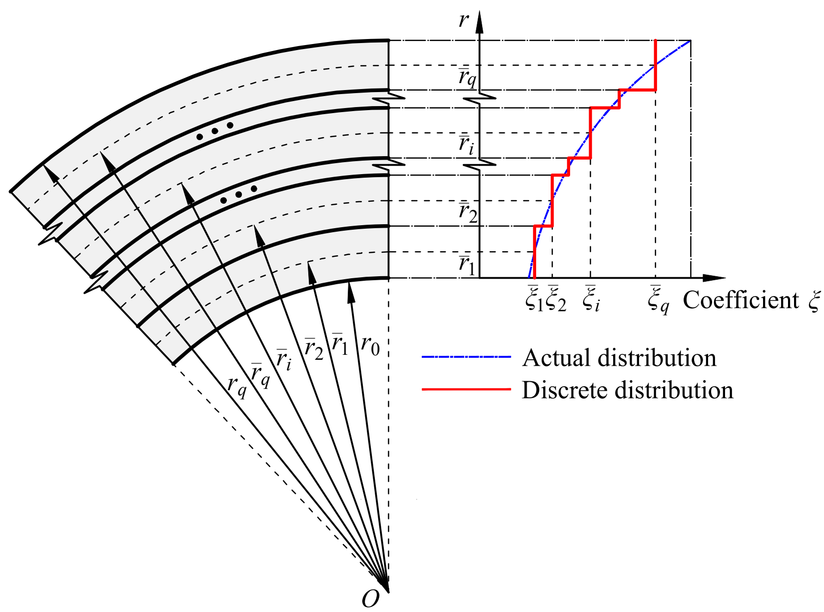

Figure 3. Approximation of the r-dependent coefficients.

3. Temperature Solution

Based on the arched-slice model, an iteration approach will be applied to solve the nonlinear heat conduction equations for the TD case (i.e., the thermomechanical properties of the arch are TD). Before introducing the iteration procedure, we first give an exact solution of the heat conduction equations for the TI case (i.e., the thermomechanical properties are assumed to be TI).

3.1. Temperature Solution for the TI Case

The temperature field in the TI case is governed by the following.

(i) Heat conduction of the ith (i = 1, 2, . . ., q) slice across the r-direction,

$$\frac{dT_i}{dr} + r\frac{d^2T_i}{dr^2} = 0 \tag{1}$$

(ii) Temperature and flux at the interface between the ith (i = 1, 2, . . ., $q - 1$) and (i + 1)th slices,

$$\left\{ \begin{array}{c} T_i \\ \bar{k}_i \frac{dT_i}{dr} \end{array} \right\}_{r = r_i} = \left\{ \begin{array}{c} T_{i+1} \\ \bar{k}_{i+1} \frac{dT_{i+1}}{dr} \end{array} \right\}_{r = r_i} \tag{2}$$

(iii) Inside and outside surface temperatures,

$$\left\{ \begin{array}{c} T_1(r_0) \\ T_q(r_q) \end{array} \right\} = \left\{ \begin{array}{c} T_{in} \\ T_{out} \end{array} \right\} \tag{3}$$

Using Equations (1)–(3) yields the following temperature solution:

$$T_i = \frac{A_i + \frac{\bar{k}_1}{\bar{k}_i} \ln r}{A_q + \frac{\bar{k}_1}{\bar{k}_q} \ln r_q} (T_{out} - T_{in}) + T_{in} \tag{4}$$

where

$$A_\xi = \bar{k}_1 \sum_{j = 2}^{\xi} \left(\frac{\ln r_{j-1}}{\bar{k}_{j-1}} - \frac{\ln r_{j-1}}{\bar{k}_j} \right) - \ln r_0,\ \xi = i,\ q \tag{5}$$

3.2. Temperature Solution for the TD Case

According to the exact solution Equation (4), we further use the iteration approach to solve the heat conduction problem for the TD case. To implement the iteration approach, an initial solution should be assumed. Here, we assume that the temperature is initially a linear function of r. The iteration procedure is shown in Figure 4.

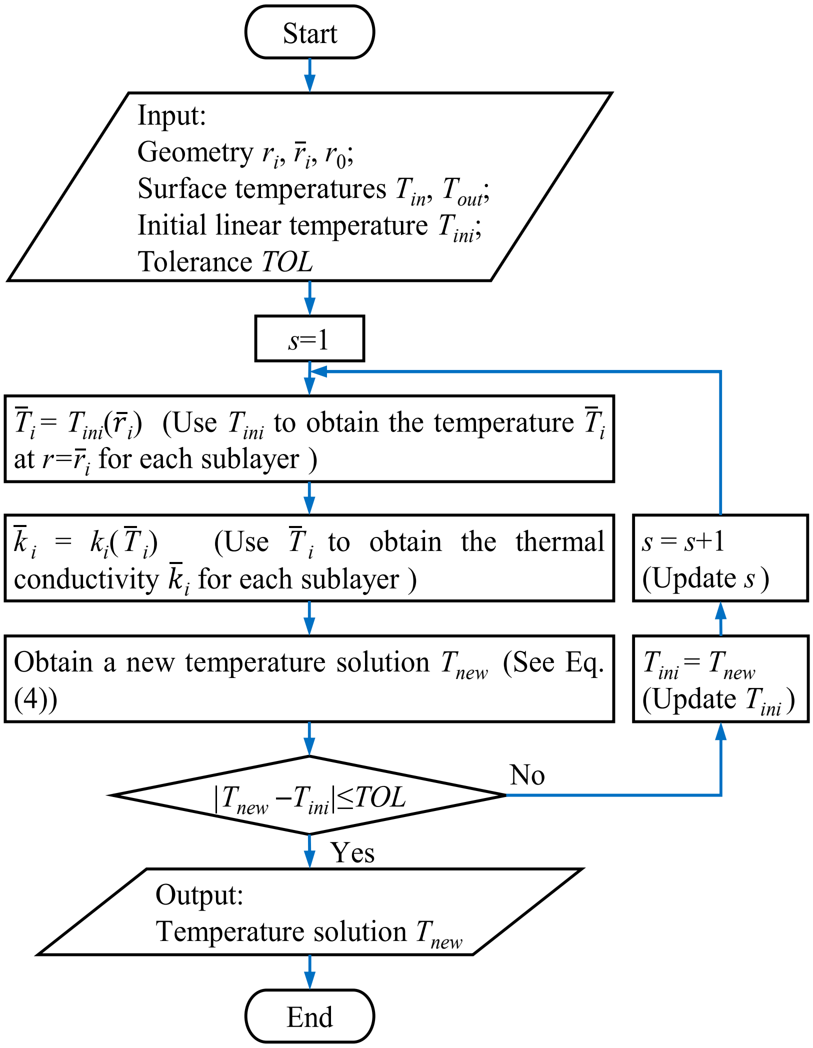

Figure 4. Iteration procedure of temperature solution.

4. Displacement and Stress Solutions

In Section 3, we obtained the temperature solution, which can be used for the displacement and stress analyses in this section.

4.1. Basic Equations

Based on the two-dimensional thermoelasticity theory, the deformed state of the arch is governed by the following [47].

(i) Equilibrium equation of the ith ($i = 1, 2, \ldots, q$) slice,

$$\frac{\partial \sigma_r^i}{\partial r} + \frac{1}{r}\frac{\partial \tau_{\varphi r}^i}{\partial \varphi} + \frac{\sigma_r^i - \sigma_\varphi^i}{r} = 0, \ \frac{1}{r}\frac{\partial \sigma_\varphi^i}{\partial \varphi} + \frac{\partial \tau_{\varphi r}^i}{\partial r} + \frac{2\tau_{\varphi r}^i}{r} = 0 \tag{6}$$

(ii) Strain–displacement relation,

$$\varepsilon_\varphi^i = \frac{u_r^i}{r} + \frac{1}{r}\frac{\partial u_\varphi^i}{\partial \varphi}, \ \varepsilon_r^i = \frac{\partial u_r^i}{\partial r}, \ \gamma_{\varphi r}^i = \frac{1}{r}\frac{\partial u_r^i}{\partial \varphi} + \frac{\partial u_\varphi^i}{\partial r} - \frac{u_\varphi^i}{r} \tag{7}$$

(iii) Stress–strain relation in the plane-stress condition,

$$\begin{Bmatrix} \sigma_\varphi^i \\ \sigma_r^i \\ \tau_{\varphi r}^i \end{Bmatrix} = \begin{bmatrix} \frac{\overline{E}_i}{1-\overline{\mu}_i^2} & \frac{\overline{E}_i\overline{\mu}_i}{1-\overline{\mu}_i^2} & 0 \\ \frac{\overline{E}_i\overline{\mu}_i}{1-\overline{\mu}_i^2} & \frac{\overline{E}_i}{1-\overline{\mu}_i^2} & 0 \\ 0 & 0 & \frac{\overline{E}_i}{2(1+\overline{\mu}_i)} \end{bmatrix} \begin{Bmatrix} \varepsilon_\varphi^i \\ \varepsilon_r^i \\ \gamma_{\varphi r}^i \end{Bmatrix} - \begin{Bmatrix} t_i \\ t_i \\ 0 \end{Bmatrix} \tag{8}$$

where $t_i = \overline{E}_i\overline{\alpha}_i(\overline{T}_i - T_0)/(1-\overline{\mu}_i)$.

(iv) Displacements and stresses at the interface between the ith (i = 1, 2, . . ., $q-1$) and (i + 1)th slices,

$$\begin{Bmatrix} u_\varphi^i \\ u_r^i \\ \tau_{\varphi r}^i \\ \sigma_r^i \end{Bmatrix}_{r\,=\,r_i} = \begin{Bmatrix} u_\varphi^{i+1} \\ u_r^{i+1} \\ \tau_{\varphi r}^{i+1} \\ \sigma_r^{i+1} \end{Bmatrix}_{r\,=\,r_i} \tag{9}$$

(v) Inside and outside surface stresses,

$$\begin{Bmatrix} \sigma_r^1 \\ \tau_{\varphi r}^1 \end{Bmatrix}_{r\,=\,r_0} = \mathbf{0},\ \begin{Bmatrix} \sigma_r^q \\ \tau_{\varphi r}^q \end{Bmatrix}_{r\,=\,r_q} = \begin{Bmatrix} -Q(\varphi) \\ 0 \end{Bmatrix} \tag{10}$$

(vi) Simply supported boundary conditions,

$$\begin{Bmatrix} u_r^i \\ \sigma_\varphi^i \end{Bmatrix}_{\varphi\,=\,0,\theta} = \mathbf{0} \tag{11}$$

Applying the state-space approach [48] to Equations (6)–(8) yields

$$\frac{\partial}{\partial r}\begin{Bmatrix} u_\varphi^i \\ \sigma_r^i \\ \tau_{\varphi r}^i \\ u_r^i \end{Bmatrix} = \begin{bmatrix} \frac{1}{r} & 0 & \frac{2(1+\overline{\mu}_i)}{\overline{E}_i} & -\frac{1}{r}\frac{\partial}{\partial\varphi} \\ \frac{\overline{E}_i}{r^2}\frac{\partial}{\partial\varphi} & \frac{\overline{\mu}_i-1}{r} & -\frac{1}{r}\frac{\partial}{\partial\varphi} & \frac{\overline{E}_i}{r^2} \\ -\frac{\overline{E}_i}{r^2}\frac{\partial^2}{\partial\varphi^2} & -\frac{\overline{\mu}_i}{r}\frac{\partial}{\partial\varphi} & -\frac{2}{r} & -\frac{\overline{E}_i}{r^2}\frac{\partial}{\partial\varphi} \\ -\frac{\overline{\mu}_i}{r}\frac{\partial}{\partial\varphi} & \frac{1-\overline{\mu}_i{}^2}{\overline{E}_i} & 0 & -\frac{\overline{\mu}_i}{r} \end{bmatrix} \begin{Bmatrix} u_\varphi^i \\ \sigma_r^i \\ \tau_{\varphi r}^i \\ u_r^i \end{Bmatrix} + \begin{Bmatrix} 0 \\ \frac{\overline{\mu}_i-1}{r}t_i \\ -\frac{\overline{\mu}_i-1}{r}\frac{\partial t_i}{\partial\varphi} \\ \frac{1-\overline{\mu}_i{}^2}{\overline{E}_i}t_i \end{Bmatrix} \tag{12}$$

The induced stress σ_φ^i can be obtained as

$$\sigma_\varphi^i = \overline{\mu}_i\left(\sigma_r^i + t_i\right) + \frac{\overline{E}_i}{r}u_r^i + \frac{\overline{E}_i}{r}\frac{\partial u_\varphi^i}{\partial\varphi} - t_i \tag{13}$$

4.2. General Solution to the Thermoelasticity Equations

Given that the coefficient matrix of Equation (12) has the variable r, it is impractical to exactly solve the equation. Here, we can replace the variable coefficient matrix with a constant one by setting $r = \overline{r}_i$. It should be mentioned that the error induced by the replacement is negligible due to the thinness of every slice. Under this circumstance, Equations (12) and (13) can be approximated as

$$\frac{\partial}{\partial r}\begin{Bmatrix} u_\varphi^i \\ \sigma_r^i \\ \tau_{\varphi r}^i \\ u_r^i \end{Bmatrix} = \begin{bmatrix} \frac{1}{\overline{r}_i} & 0 & \frac{2(1+\overline{\mu}_i)}{\overline{E}_i} & -\frac{1}{\overline{r}_i}\frac{\partial}{\partial\varphi} \\ \frac{\overline{E}_i}{\overline{r}_i{}^2}\frac{\partial}{\partial\varphi} & \frac{\overline{\mu}_i-1}{\overline{r}_i} & -\frac{1}{\overline{r}_i}\frac{\partial}{\partial\varphi} & \frac{\overline{E}_i}{\overline{r}_i{}^2} \\ -\frac{\overline{E}_i}{\overline{r}_i{}^2}\frac{\partial^2}{\partial\varphi^2} & -\frac{\overline{\mu}_i}{\overline{r}_i}\frac{\partial}{\partial\varphi} & -\frac{2}{\overline{r}_i} & -\frac{\overline{E}_i}{\overline{r}_i{}^2}\frac{\partial}{\partial\varphi} \\ -\frac{\overline{\mu}_i}{\overline{r}_i}\frac{\partial}{\partial\varphi} & \frac{1-\overline{\mu}_i^2}{\overline{E}_i} & 0 & -\frac{\overline{\mu}_i}{\overline{r}_i} \end{bmatrix}\begin{Bmatrix} u_\varphi^i \\ \sigma_r^i \\ \tau_{\varphi r}^i \\ u_r^i \end{Bmatrix} + \begin{Bmatrix} 0 \\ \frac{\overline{\mu}_i-1}{\overline{r}_i}t_i \\ -\frac{\overline{\mu}_i-1}{\overline{r}_i}\frac{\partial t_i}{\partial\varphi} \\ \frac{1-\overline{\mu}_i{}^2}{\overline{E}_i}t_i \end{Bmatrix} \quad (14)$$

$$\sigma_\varphi^i = \overline{\mu}_i\left(\sigma_r^i + t_i\right) + \frac{\overline{E}_i}{\overline{r}_i}u_r^i + \frac{\overline{E}_i}{\overline{r}_i}\frac{\partial u_\varphi^i}{\partial\varphi} - t_i \quad (15)$$

To satisfy the simply supported conditions in Equation (11), we assume the solutions of Equation (14) as

$$\begin{Bmatrix} u_\varphi^i \\ u_r^i \\ \tau_{\varphi r}^i \\ \sigma_r^i \end{Bmatrix} = \sum_{m=1}^{\infty}\begin{Bmatrix} U_m^i(r)\cos(\beta_m\varphi) \\ W_m^i(r)\sin(\beta_m\varphi) \\ \Gamma_m^i(r)\cos(\beta_m\varphi) \\ R_m^i(r)\sin(\beta_m\varphi) \end{Bmatrix} \quad (16)$$

where $\beta_m = \frac{m\pi}{\theta}$ and $U_m^i(r)$, $W_m^i(r)$, $\Gamma_m^i(r)$, and $R_m^i(r)$ are unknowns.

The stress t_i in Equation (14) can be expanded as

$$t_i(\varphi) = \sum_{r=1}^{\infty} t_m^i \sin(\beta_m\varphi) \quad (17)$$

where $t_m^i = \frac{2}{\theta}\int_0^\theta t_i \sin(\beta_m\varphi)d\varphi$.

Using Equations (16) and (17), the partial differential equation shown in Equation (14) can be reduced to an ordinary differential one as follows:

$$\frac{d\boldsymbol{\delta}_i(r)}{dr} = \boldsymbol{M}_i\boldsymbol{\delta}_i(r) + \boldsymbol{N}_i \quad (18)$$

where

$$\boldsymbol{\delta}_i(r) = \begin{Bmatrix} U_m^i(r) \\ R_m^i(r) \\ \Gamma_m^i(r) \\ W_m^i(r) \end{Bmatrix}, \boldsymbol{M}_i = \begin{bmatrix} \frac{1}{\overline{r}_i} & 0 & \frac{2(1+\overline{\mu}_i)}{\overline{E}_i} & -\frac{1}{\overline{r}_i}\beta_m \\ -\frac{\overline{E}_i}{\overline{r}_i^2}\beta_m & \frac{\overline{\mu}_i-1}{\overline{r}_i} & \frac{1}{\overline{r}_i}\beta_m & \frac{\overline{E}_i}{\overline{r}_i^2} \\ \frac{\overline{E}_i}{\overline{r}_i^2}\beta_m^2 & -\frac{\overline{\mu}_i}{\overline{r}_i}\beta_m & -\frac{2}{\overline{r}_i} & -\frac{\overline{E}_i}{\overline{r}_i^2}\beta_m \\ \frac{\overline{\mu}_i}{\overline{r}_i}\beta_m & \frac{1-\overline{\mu}_i{}^2}{\overline{E}_i} & 0 & -\frac{\overline{\mu}_i}{\overline{r}_i} \end{bmatrix}, \boldsymbol{N}_i = \begin{Bmatrix} 0 \\ \frac{\overline{\mu}_i-1}{\overline{r}_i}t_m^i \\ \frac{1-\overline{\mu}_i}{\overline{r}_i}\beta_m t_m^i \\ \frac{1-\overline{\mu}_i{}^2}{\overline{E}_i}t_m^i \end{Bmatrix} \quad (19)$$

Similarly, substituting Equations (16) and (17) into Equation (15) gives

$$\sigma_\varphi^i = \sum_{m=1}^{\infty}\left[\overline{\mu}_i R_m^i(r) + (\overline{\mu}_i - 1)t_m^i + \frac{\overline{E}_i}{\overline{r}_i}W_m^i(r) - \frac{\overline{E}_i}{\overline{r}_i}\beta_m U_m^i(r)\right]\sin(\beta_m\varphi) \quad (20)$$

Based on the matrix theory, the general solution to Equation (18) is [48]

$$\boldsymbol{\delta}_i(r) = \boldsymbol{A}_i(r-r_{i-1})\boldsymbol{\delta}_i(r_{i-1}) + \boldsymbol{B}_i(r-r_{i-1}),\ r\in[r_{i-1},\ r_i] \quad (21)$$

where

$$\boldsymbol{A}_i(r-r_{i-1}) = \exp[\boldsymbol{M}_i(r-r_{i-1})],\ \boldsymbol{B}_i(r-r_{i-1}) = \exp[\boldsymbol{M}_i(r-r_{i-1})]\boldsymbol{M}_i^{-1}\boldsymbol{N}_i - \boldsymbol{M}_i^{-1}\boldsymbol{N}_i \quad (22)$$

4.3. Transfer-Matrix Approach

The radial load $Q(\varphi)$ can be expanded as

$$Q(\varphi) = \sum_{m=1}^{\infty} Q_m \sin(\beta_m \varphi) \tag{23}$$

where $Q_m = \frac{2}{\theta}\int_0^{\theta} Q(\varphi)\sin(\beta_m \varphi)d\varphi$.

Substituting Equations (16) and (23) into the boundary conditions in Equations (9) and (10) yields

$$\delta_{i+1}(r_i) = \delta_i(r_i) \tag{24}$$

$$\delta_1(r_0) = \left\{ U_m^1(r_0) \quad 0 \quad 0 \quad W_m^1(r_0) \right\}^T,\ \delta_q(r_q) = \left\{ U_m^q(r_q) \quad -Q_m \quad 0 \quad W_m^q(r_q) \right\}^T \tag{25}$$

Substituting $r = r_i$ into Equation (21) yields

$$\delta_i(r_i) = \boldsymbol{A}_i(h_i)\delta_i(r_{i-1}) + \boldsymbol{B}_i(h_i) \tag{26}$$

Based on the continuity condition Equation (24) at all the interfaces and using the transfer-matrix approach, the following relations can be obtained:

$$\delta_i(r_i) = \prod_{s=i}^{1}[\boldsymbol{A}_s(h_s)]\delta_1(r_0) + \sum_{s=1}^{i-1}\left\{\prod_{j=i}^{s+1}[\boldsymbol{A}_j(h_j)]\boldsymbol{B}_s(h_s)\right\} + \boldsymbol{B}_i(h_i),\ i = 1, 2, \ldots, q \tag{27}$$

Incorporating the boundary condition Equation (25) into Equation (27) yields

$$\left\{ U_m^q(r_q) \quad -Q_m \quad 0 \quad W_m^q(r_q) \right\}^T = \boldsymbol{S}\left\{ U_m^1(r_0) \quad 0 \quad 0 \quad W_m^1(r_0) \right\}^T + \overline{\boldsymbol{S}} \tag{28}$$

where

$$\boldsymbol{S} = \begin{bmatrix} S_{11} & \cdots & S_{14} \\ \vdots & \ddots & \vdots \\ S_{41} & \cdots & S_{44} \end{bmatrix} = \prod_{i=q}^{1}\boldsymbol{A}_i(h_i),\ \overline{\boldsymbol{S}} = \left\{ \overline{S}_1 \quad \cdots \quad \overline{S}_4 \right\}^T = \sum_{i=1}^{q-1}\left\{\prod_{j=q}^{i+1}[\boldsymbol{A}_j(h_j)]\boldsymbol{B}_i(h_i)\right\} + \boldsymbol{B}_q(h_q) \tag{29}$$

Decomposing Equation (28) gives the solution of $U_m^1(r_0)$ and $W_m^1(r_0)$ as follows:

$$\begin{Bmatrix} U_m^1(r_0) \\ W_m^1(r_0) \end{Bmatrix} = -\begin{bmatrix} S_{21} & S_{24} \\ S_{31} & S_{34} \end{bmatrix}^{-1}\begin{Bmatrix} Q_m + \overline{S}_2 \\ \overline{S}_3 \end{Bmatrix} \tag{30}$$

Substituting Equation (30) into Equation (25) yields $\delta_1(r_0)$. Incorporating $\delta_1(r_0)$ into Equation (27) and using the continuity condition Equation (24) yields $\delta_i(r_{i-1})$. Incorporating $\delta_i(r_{i-1})$ into Equation (21) gives $\delta_i(r)$ for every slice. Finally, the displacements u_φ^i and u_r^i and stresses σ_φ^i, σ_r^i and $\tau_{\varphi r}^i$ are obtained from Equations (16) and (20).

The present method focuses on arches with simply supported ends. The method can also be developed to deal with other support conditions. For example, the clamped end can be transformed into a simply supported one by adding the unknown longitudinal surface forces, which can be finally determined by the zero displacement condition at the end [49].

5. Numerical Results and Discussion

Numerical examples were conducted to study the thermoelastic behaviors of a steel-concrete-steel sandwich arch. Table 1 lists the Young's moduli of steel and concrete at different temperatures [50,51]. Table 2 shows the thermal conductivities, thermal expansion coefficients, and Poisson's ratios, which are all expressed by quadratic polynomials as $P(T) = P_2T^2 + P_1T + P_0$. Unless otherwise stated, some of the geometry and load parameters are fixed at $H_1 = H_3 = 0.1H$, $Q(\varphi) = 5000$ N/m, $T_{in} = T_0 = 20$°C, while the outside surface temperature T_{out}, thickness H, angle θ, mean radius r_m ($r_m = 0.5(r_0 + r_q)$), and mean length L ($L = \theta r_m$) are the variables. Given that the present method is based on the arched-slice model, we assumed that the arch was divided into q arched slices with equal thickness.

Table 1. Young's moduli of steel and concrete at different temperatures [50,51].

T **(°C)**	**20**	**100**	**150**	**200**	**300**	**400**	**500**	**600**	**700**
E_s (GPa)	210	210	-	189	168	147	126	65.1	27.3
E_c (GPa)	30	30	30	-	-	-	-	-	0

Note: Linear interpolation is applied to obtain Young's moduli at other temperatures.

Table 2. Temperature-dependent coefficients for steel and concrete [50,51].

P(T)	P_2	P_1	P_0
k_s (W/m°C)	-3.33×10^{-2}	0	54
k_c (W/m°C)	5.7×10^{-7}	-3.36×10^{-3}	1.36
α_s (°C^{-1})	0	4×10^{-9}	1.208×10^{-5}
α_c (°C^{-1})	1.4×10^{-11}	2.8×10^{-10}	6.0056×10^{-6}
μ_s	0	0	0.3
μ_c	0	0	0.2

5.1. Validation of the Solutions

The convergence and accuracy of the present method were studied. Firstly, we considered the sandwich arch ($\theta = 0.5\pi$ rad, $r_m = 1.1$ m, $H = 0.2$ m) heated at $T_{out} = 200$ °C. Tables 3 and 4 show the convergence results for the temperature, displacement, and stress solutions, as well as the comparison with the finite element (FE) solutions. In Table 4, u_φ^r denotes u_φ at $\varphi = 0$, $r = r_m$; u_r^m denotes u_r at $\varphi = 0.5\theta$, $r = r_m$; and σ_φ^m denotes σ_φ at $\varphi = 0.5\theta$, $r = r_m$. The FE analysis was conducted using the commercial package ABAQUS. The four-node heat element, DC2D4, and the four-node plane stress element, CPS4R, were applied to model the arch. Given the symmetry, we only modelled half of the arch, as shown in Figure 5. The FE solutions were obtained by dividing the face and core layers with 4 and 16 elements along the r-direction, respectively, and 50 elements along the φ-direction. It can be seen from Tables 3 and 4 that the present solutions converge quickly with the increase of the slice number q, iterative step s, and half wave number m. The FE solutions match well with the present ones.

Table 3. Convergence and comparison study of the temperature solutions (unit: °C).

Positions	**FE Solutions**	**Present Solutions**				
			$s = 1$	$s = 2$	$s = 3$	$s = 4$
$r = 1.05$ m	53.660	$q = 10$	54.184	53.714	53.723	53.723
		$q = 20$	54.133	53.652	53.661	53.661
		$q = 50$	54.135	53.654	53.663	53.664
		$q = 100$	54.133	53.652	53.661	53.661
		$q = 200$	54.133	53.652	53.661	53.661

Table 3. *Cont.*

Positions	FE Solutions	Present Solutions				
			s = 1	s = 2	s = 3	s = 4
r = 1.1 m	109.212	q = 10	110.006	109.214	109.214	109.214
		q = 20	110.006	109.214	109.214	109.214
		q = 50	110.006	109.214	109.214	109.214
		q = 100	110.006	109.214	109.214	109.214
		q = 200	110.006	109.214	109.214	109.214
r = 1.15 m	165.390	q = 10	165.940	165.465	165.456	165.456
		q = 20	165.888	165.400	165.391	165.391
		q = 50	165.890	165.403	165.394	165.394
		q = 100	165.888	165.400	165.391	165.391
		q = 200	165.888	165.400	165.391	165.391

Table 4. Convergence and comparison study of the displacement and stress solutions.

Variables	FE Solutions	Present Solutions					
			m = 5	m = 25	m = 45	m = 65	m = 85
u_φ^r(mm)	2.15	q = 10	2.17	2.15	2.14	2.14	2.14
		q = 50	2.18	2.15	2.15	2.15	2.15
		q = 100	2.18	2.15	2.15	2.15	2.15
		q = 200	2.18	2.15	2.15	2.15	2.15
		q = 400	2.18	2.15	2.15	2.15	2.15
		q = 600	2.18	2.15	2.15	2.15	2.15
u_r^m(mm)	5.68	q = 10	5.68	5.67	5.67	5.67	5.67
		q = 50	5.69	5.68	5.68	5.68	5.68
		q = 100	5.69	5.68	5.68	5.68	5.68
		q = 200	5.69	5.68	5.68	5.68	5.68
		q = 400	5.69	5.68	5.68	5.68	5.68
		q = 600	5.69	5.68	5.68	5.68	5.68
σ_φ^m(MPa)	12.7	q = 10	10.3	10.2	10.2	10.2	10.2
		q = 50	12.5	12.2	12.3	12.3	12.3
		q = 100	12.8	12.5	12.5	12.5	12.5
		q = 200	12.9	12.6	12.6	12.6	12.6
		q = 400	13.0	12.7	12.7	12.7	12.7
		q = 600	13.0	12.7	12.7	12.7	12.7

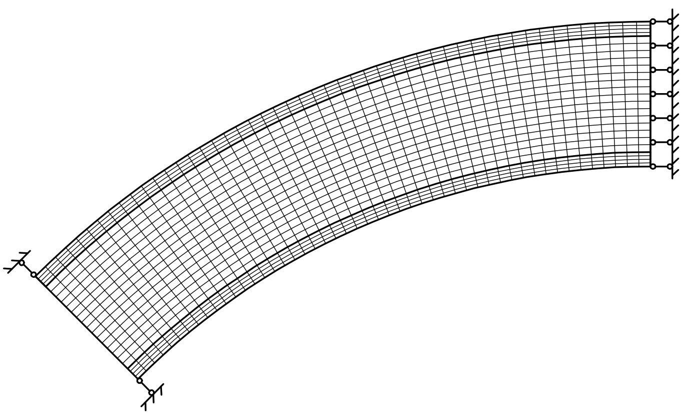

Figure 5. FE model of the sandwich arch.

The sandwich arch can also be studied using the EBT [19]. Here, the deflections u_r^m of the arch ($Q(\varphi)$ = 0, T_{out} = 400 °C) obtained using EBT and thermoelasticity theory are compared. Figure 6a shows the effects of the length-to-thickness ratio L/H on the comparison results when the angle and mean radius are fixed at θ = 0.3π rad and r_m = 10 m, respectively; Figure 6b displays the effects of the angle θ on the comparative results when L/H = 10 and r_m = 10 m; and Figure 6c displays the effects of the curvature $1/r_m$ on the comparative results when L/H = 10 and θ = 0.3π rad. We can see that the EBT solutions match well with the present ones for thin and shallow arches, but the error of the EBT increases when L/H decreases or θ increases; the curvature $1/r_m$ almost does not affect the accuracy of the EBT solutions.

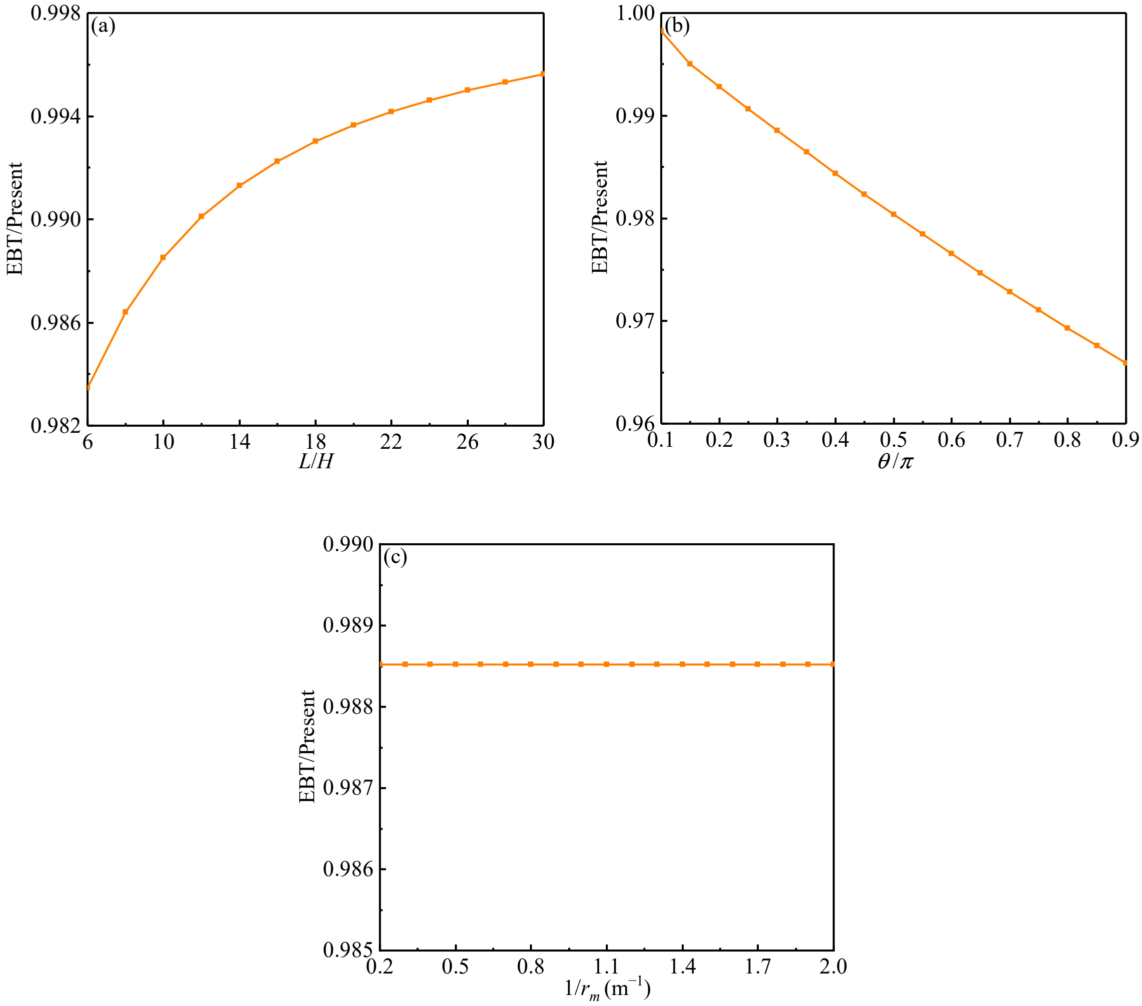

Figure 6. Effects of (**a**) length-to-thickness ratio L/H, (**b**) angle θ, and (**c**) curvature $1/r_m$ on the deflections obtained using EBT and thermoelasticity theory.

5.2. Parametric Study

We considered the sandwich arch (θ = 0.75π, r_m = 1.1 m, H = 0.2 m) heated with T_{out} = 100 °C, 200 °C, and 300 °C. The temperature, displacement, and stress distributions of the arch in the TD and TI cases are both considered for comparison. Note that the reference temperature, T_0 = 20 °C, was used to determine the thermomechanical properties for the TI case.

5.2.1. Temperature Distribution

Figure 7 shows the temperature distributions across the thickness for the TD and TI cases. We found that T changes rapidly in the concrete layer, but is almost invariable in the steel layer, given that k_c is much smaller than k_s. By increasing T_{out}, the difference of T in the concrete layer between the TD and TI cases increases. To further illustrate the effects of T_{out} and temperature dependency of thermomechanical properties on the temperature field of the arch, we show the relation between T_{out} and T at $r = r_m$, considering both the

TD and TI cases, in Figure 8. We can see that T nonlinearly changes with T_{out} in the TD case, but linearly changes with T_{out} in the TI case. When T_{out} = 300 °C, the difference in T between the two cases is 6.38%.

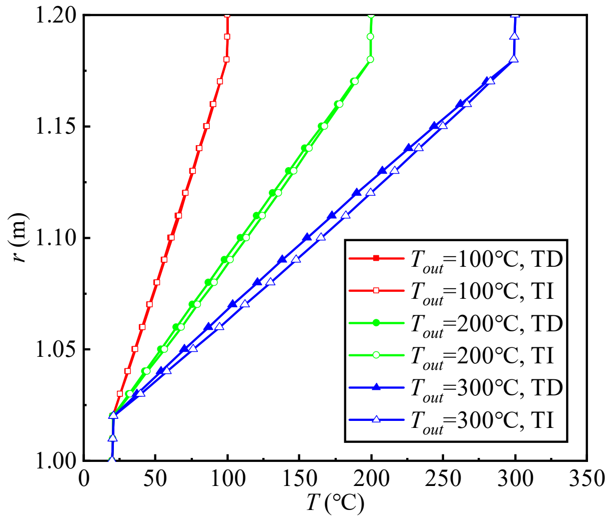

Figure 7. Temperature distributions across the thickness of the sandwich arch.

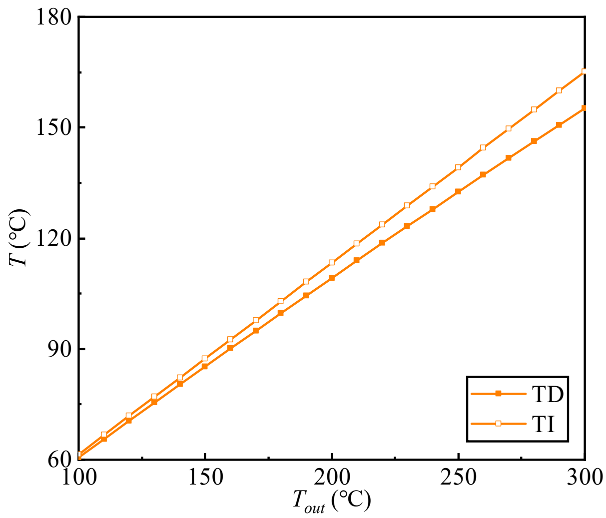

Figure 8. Temperature at $r = r_m$ vs. the outside surface temperature T_{out}.

5.2.2. Displacement and Stress Distributions

Given that the arch considered in this work is under combined thermal and mechanical loadings, here we separately study the mechanical responses induced by the two kinds of loadings. Note that whether the arch is under thermal loading or mechanical loading, the TD and TI cases are considered to show the effects of temperature dependency of thermomechanical properties on the induced mechanical responses.

Firstly, the displacements and stresses induced by thermal loading were studied. Figure 9 shows the distributions of u_φ^T at $\varphi = 0$ and u_r^T and σ_φ^T at $\varphi = 0.5\theta$ for the TD and TI cases, where the superscript T indicates the thermal loading. It is seen that, by increasing T_{out}, the difference of displacement and stress distributions between the two cases increases. Figure 9a,b show that, for any fixed T_{out}, the TD case has a larger deformation compared with the TI case, because the high-temperature environment can degrade the stiffness of the arch when considering the temperature dependency of thermomechanical properties. Figure 9c shows that, because of the mismatch of thermomechanical properties between the face and core layers, σ_φ^T is discontinuous at the interfaces.

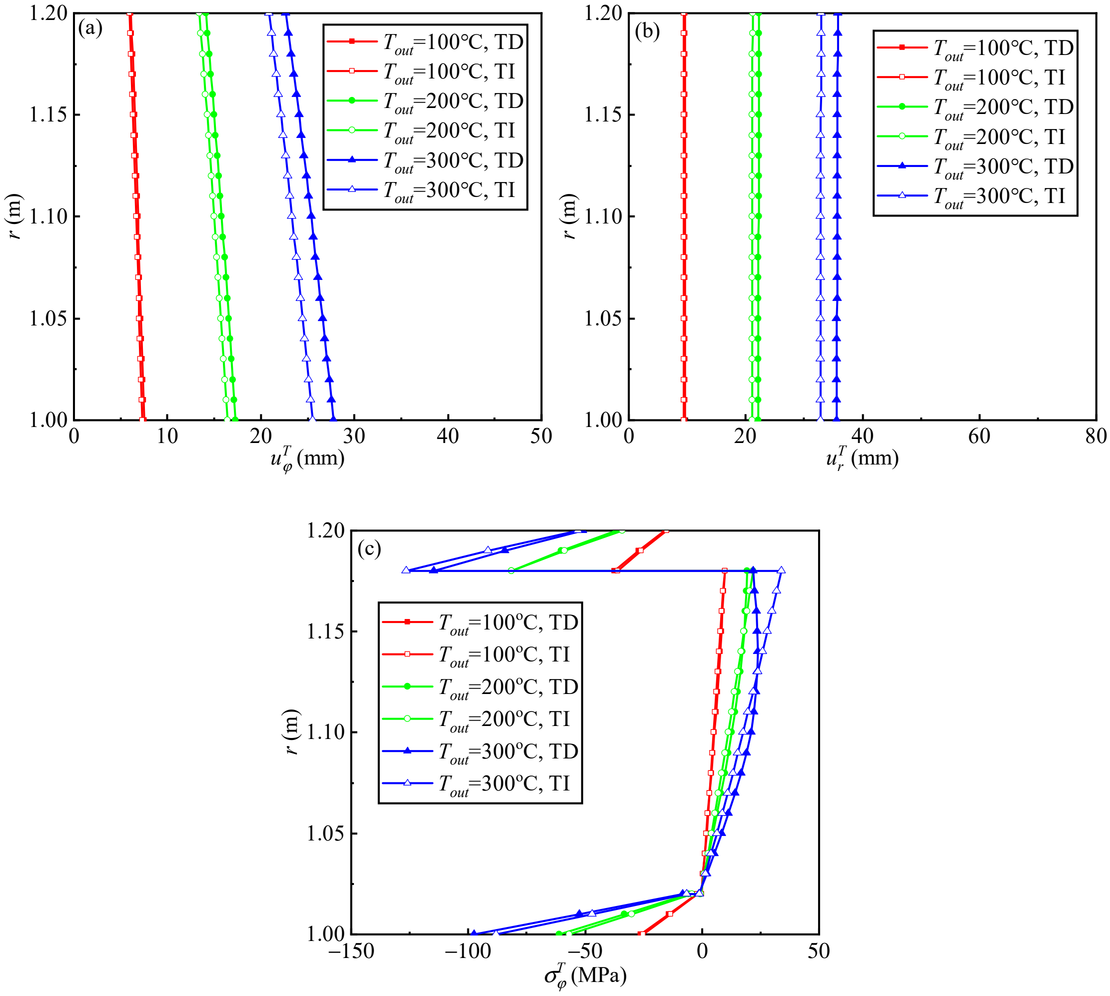

Figure 9. Distributions of displacements and stresses induced by thermal loading: (**a**) u_φ^T at $\varphi = 0$; (**b**) u_r^T at $\varphi = 0.5\theta$; and (**c**) σ_φ^T at $\varphi = 0.5\theta$.

Figure 10 shows u_r^T and σ_φ^T at $\varphi = 0.5\theta$ and $r = r_q$ vs. T_{out}, considering both the TD and TI cases. We can see that u_r^T and σ_φ^T nonlinearly change with T_{out} in the TD case, but linearly change with T_{out} in the TI case. The phenomenon is similar to that of temperature, as shown in Figure 8. It was also found that u_r^T in the TD case is always larger than that in the TI case for any fixed T_{out}. However, σ_φ^T in the TD case is not always larger than that in the TI case with the increase of T_{out}. When $T_{out} = 300$ °C, the differences between the two cases are 7.96% and 4.20% for u_r^T and σ_φ^T, respectively. By combining Figures 8 and 10, it is concluded that the temperature dependency of thermomechanical properties is a key parameter in predicting the thermoelastic behaviors of the arch in high-temperature environments.

Secondly, the displacements and stresses induced by mechanical loading were studied. Figure 11 shows the distributions of u_r^M and σ_φ^M at $\varphi = 0.5\theta$ and $\tau_{\varphi r}^M$ at $\varphi = 0$ for the TD and TI cases, where the superscript M indicates the mechanical loading. It is shown that when $T_{out} = 100$ °C, the TD and TI cases have the same displacement and stress distributions, given that the thermomechanical properties (Young's modulus and Poisson's ratio) of the constituents remain constant when $T \leq 100$°C (see Tables 1 and 2). It is also noticed that in the TD case, u_r^M increases with T_{out}, because the stiffness of the arch is degraded with T_{out}; however, the distributions of σ_φ^M and $\tau_{\varphi r}^M$ are almost unchanged with the increase of T_{out}. Furthermore, Figures 9 and 11 show that the deformations and stresses induced by thermal loading are much bigger than those induced by mechanical loading. Hence, thermal loading has a major influence on the mechanical behaviors of the arch in this study.

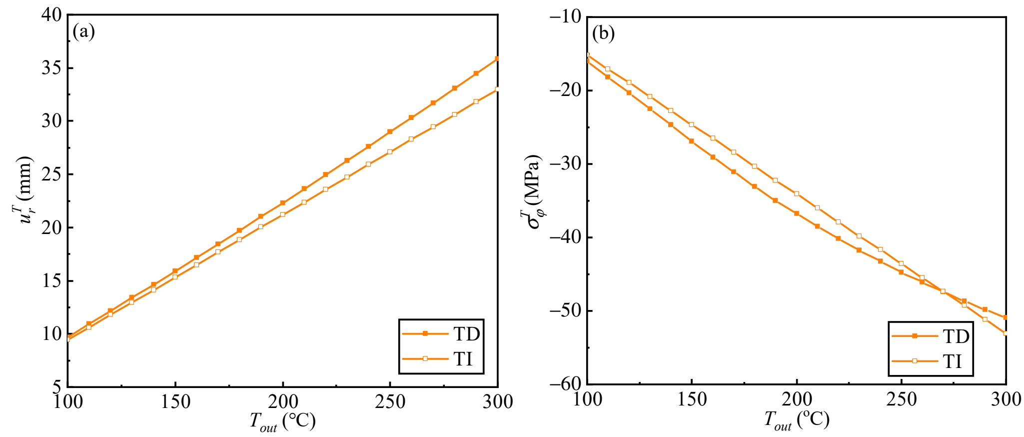

Figure 10. Displacements and stresses induced by thermal loading vs. the outside surface temperature T_{out}: (**a**) u_r^T at $\varphi = 0.5\theta$ and $r = r_q$; and (**b**) σ_φ^T at $\varphi = 0.5\theta$ and $r = r_q$.

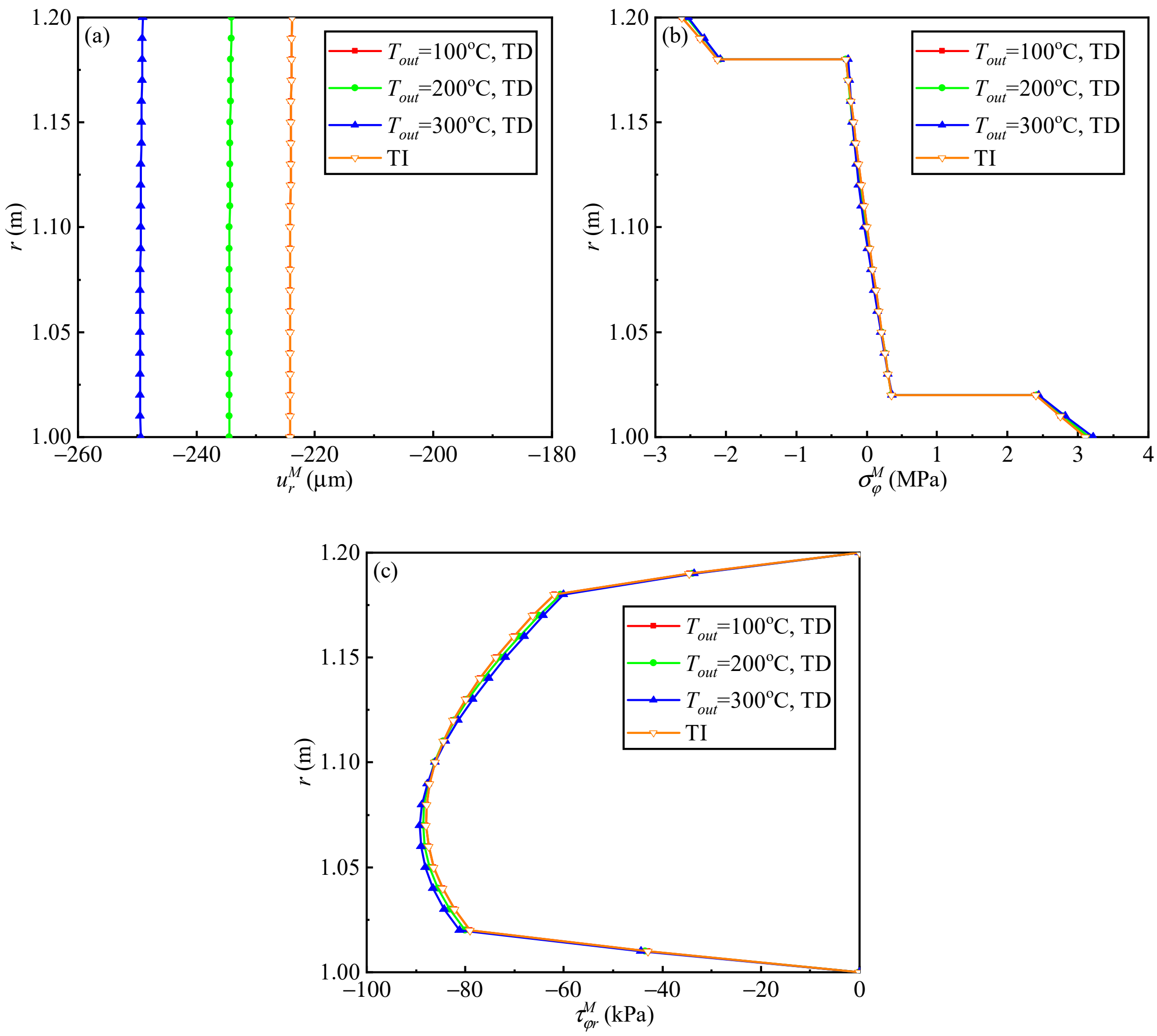

Figure 11. Distributions of displacements and stresses induced by mechanical loading: (**a**) u_r^M at $\varphi = 0.5\theta$; (**b**) σ_φ^M at $\varphi = 0.5\theta$; and (**c**) $\tau_{\varphi r}^M$ at $\varphi = 0$.

6. Conclusions

An arched-slice model is proposed to study the thermoelastic behaviors of TD multilayer arches under thermomechanical loadings. Based on the model, the temperature solution is obtained by applying the iteration approach to the nonlinear heat conduction equations, and then the displacement and stress solutions are obtained by applying the state-space approach and transfer-matrix approach to the two-dimensional thermoelasticity equations. The convergence and accuracy of the present solutions were studied. The effects of surface temperature and TD thermomechanical properties on the temperature, displacement, and stress distributions of a sandwich arch are studied. The following findings were obtained.

i. The present solutions converge quickly with high accuracy. By comparing the present solutions with those predicted by the EBT, it was found that for thin and shallow arches, the deflection predicted by the EBT agrees well with that predicted by the present thermoelasticity theory. However, the error of the EBT increases when the angle θ increases or the length-to-thickness ratio L/H decreases.
ii. The temperature, displacement, and stress distributions nonlinearly change with the surface temperature in the TD case, but linearly change in the TI case.
iii. By separately studying the mechanical responses of the arch induced by thermal loading and mechanical loading, two main effects of temperature can be revealed, directly inducing thermal stresses and deformations and affecting the responses induced by mechanical loading.
iv. When the arch is subjected to thermal loading, the temperature dependence of thermomechanical properties has a much greater impact on the stress solution than on the temperature and displacement solutions.
v. Regardless of whether the arch is subjected to thermal loading or mechanical loading, the induced deformations in the TD case are always greater than those in the TI case.

Author Contributions: Conceptualization, Z.Z., Y.S. and Z.G.; methodology, Z.Z. and Y.S.; software, Z.Z. and W.Z.; validation, Y.S., W.Q. and H.G.; formal analysis, Y.S. and Z.G.; investigation, Z.Z. and W.Z.; resources, Z.G. and W.Q.; writing—original draft preparation, Z.Z., W.Z. and Y.S.; writing—review and editing, Z.Z. and Z.G.; project administration, Z.Z. and H.G.; funding acquisition, W.Q. and H.G. All authors have read and agreed to the published version of the manuscript.

Funding: This work is financially supported by the National Natural Science Foundation of China (Grant No. 52208395) and the Nantong City Social Livelihood Science and Technology Project (Grant No. MS22022067).

Data Availability Statement: Data from the study cannot be made public at this time for privacy reasons.

Conflicts of Interest: The authors declare no conflict of interest.

Nomenclature

H_j	thickness of the jth layer
k_c, α_c, E_c, μ_c	temperature-dependent thermomechanical properties of concrete
k_s, α_s, E_s, μ_s	temperature-dependent thermomechanical properties of steel
$\overline{k}_i$, $\overline{\alpha}_i$, $\overline{E}_i$, $\overline{\mu}_i$	assumed uniform thermal conductivity, thermal expansion coefficient, Young's modulus, and Poisson's ratio of the ith slice
m	number of half-waves along the φ direction
p, q	layer number and slice number
$Q(\varphi)$	radial load
r_0, r_m, r_q, H, L, θ	inside radius, mean radius, outside radius, thickness, mean length, and angle of arch
r_i, $\overline{r}_i$, h_i	outer radius, mean radius, and thickness of the ith slice
s	iterative step
T	temperature
T_0, T_{in}, T_{out}	reference temperature, inside surface temperature, and outside surface temperature
$\overline{T}_i$	assumed uniform temperature of the ith slice
u_r, u_φ	displacement components

ε_r, ε_φ, $\gamma_{\varphi r}$	strain components
σ_r, σ_φ, $\tau_{\varphi r}$	stress components
φ, r	polar coordinates

References

1. Zhou, M.; Zhuang, H.; An, L. Xuhong Bridge: A long span wooden arch bridge with glued laminated timber. *Struct. Eng. Int.* **2021**, *31*, 60–64. [CrossRef]
2. Gao, Y.; Yu, F.; Wu, P. Exact analytical solutions for bending creep behavior of viscoelastic laminated arches with interlayers. *Thin-Walled Struct.* **2022**, *174*, 109128. [CrossRef]
3. Xie, H.; Shen, C.; Fang, H.; Han, J.; Cai, W. Flexural property evaluation of web reinforced GFRP-PET foam sandwich panel: Experimental study and numerical simulation. *Compos. Part B Eng.* **2022**, *234*, 109725. [CrossRef]
4. Yan, J.B.; Liew, J.Y.R.; Zhang, M.H.; Sohel, K.M.A. Experimental and analytical study on ultimate strength behavior of steel–concrete–steel sandwich composite beam structures. *Mater. Struct.* **2015**, *48*, 1523–1544. [CrossRef]
5. Jeon, S.-J.; Jin, B.-M.; Kim, Y.-J.; Chung, C.-H. Consistent thermal analysis procedure of LNG storage tank. *Struct. Eng. Mech.* **2007**, *25*, 445–466. [CrossRef]
6. Dai, T.; Li, B.; Tao, C.; He, Z.; Huang, J. Thermo-mechanical analysis of a multilayer hollow cylindrical thermal protection structure with functionally graded ultrahigh-temperature ceramic to be heat resistant layer. *Aerosp. Sci. Technol.* **2022**, *124*, 107532. [CrossRef]
7. Shafigh, P.; Hafez, M.A.; Che Muda, Z.; Beddu, S.; Zakaria, A.; Almkahal, Z. Influence of different ambient temperatures on the thermal properties of fiber-reinforced structural lightweight aggregate concrete. *Buildings* **2022**, *12*, 771. [CrossRef]
8. Špilák, D.; Majlingová, A.; Kačíková, D.; Tischler, P. Determining the charred layer of wooden beams with finite element analysis based on enthalpy approach. *Buildings* **2022**, *12*, 875. [CrossRef]
9. Hajianmaleki, M.; Qatu, M.S. Vibrations of straight and curved composite beams: A review. *Compos. Struct.* **2013**, *100*, 218–232. [CrossRef]
10. Auciello, N.M.; De Rosa, M.A. Free vibrations of circular arches: A review. *J. Sound Vib.* **1994**, *176*, 433–458. [CrossRef]
11. Abrate, S.; Di Sciuva, M. Equivalent single layer theories for composite and sandwich structures: A review. *Compos. Struct.* **2017**, *179*, 482–494. [CrossRef]
12. Hetnarski, R.B.; Eslami, M.R. *Thermal Stresses—Advanced Theory and Applications*; Springer: Dordrecht, The Netherlands, 2009.
13. Rafiee, M.; Nitzsche, F.; Labrosse, M. Dynamics, vibration and control of rotating composite beams and blades: A critical review. *Thin-Walled Struct.* **2017**, *119*, 795–819. [CrossRef]
14. Reddy, J.N. Nonlocal theories for bending, buckling and vibration of beams. *Int. J. Eng. Sci.* **2007**, *45*, 288–307. [CrossRef]
15. Keibolahi, A.; Kiani, Y.; Eslami, M.R. Dynamic snap-through of shallow arches under thermal shock. *Aerosp. Sci. Technol.* **2018**, *77*, 545–554. [CrossRef]
16. Keibolahi, A.; Kiani, Y.; Eslami, M.R. Nonlinear rapid heating of shallow arches. *J. Therm. Stress.* **2018**, *41*, 1244–1258. [CrossRef]
17. Khalili, M.M.; Keibolahi, A.; Kiani, Y.; Eslami, M.R. Application of Ritz method to large amplitude rapid surface heating of FGM shallow arches. *Arch. Appl. Mech.* **2022**, *92*, 1287–1301. [CrossRef]
18. Keibolahi, A.; Heidari, M.; Kiani, Y.; Eslami, M.R. Nonlinear analysis of pin-ended deep arches under instantaneous heating. *J. Therm. Stress.* **2022**, *45*, 918–936. [CrossRef]
19. Khdeir, A.A. Thermally induced vibration of cross-ply laminated shallow arches. *J. Therm. Stress.* **2001**, *24*, 1085–1096. [CrossRef]
20. Rezaiee-Pajand, M.; Rajabzadeh-Safaei, N.; Hozhabrossadati, S.M. Three-dimensional deformations of a curved circular beam subjected to thermo-mechanical loading using green's function method. *Int. J. Mech. Sci.* **2018**, *142–143*, 163–175. [CrossRef]
21. Vargas, G.; Arrese, A.; Carbajal, N.; Mujika, F. Analysis of in-plane and out-of-plane thermo-mechanical stresses in un-symmetric cross-ply curved laminated strips. *J. Compos. Mater.* **2009**, *43*, 3157–3184. [CrossRef]
22. Ebrahimi, F.; Daman, M. Nonlocal thermo-electro-mechanical vibration analysis of smart curved FG piezoelectric Timoshenko nanobeam. *Smart Struct. Syst.* **2017**, *20*, 351–368. [CrossRef]
23. Bahranifard, F.; Golbahar Haghighi, M.R.; Malekzadeh, P. In-plane responses of multilayer FG-GPLRC curved beams in thermal environment under moving load. *Acta Mech.* **2020**, *231*, 2679–2696. [CrossRef]
24. Babaei, H.; Eslami, M.R. Thermally induced large deflection of FGM shallow micro-arches with integrated surface piezoelectric layers based on modified couple stress theory. *Acta Mech.* **2019**, *230*, 2363–2384. [CrossRef]
25. Sobhy, M. Differential quadrature method for magneto-hygrothermal bending of functionally graded graphene/Al sandwich-curved beams with honeycomb core via a new higher-order theory. *J. Sandw. Struct. Mater.* **2021**, *23*, 1662–1700. [CrossRef]
26. Sayyad, A.S.; Ghugal, Y.M. A sinusoidal beam theory for functionally graded sandwich curved beams. *Compos. Struct.* **2019**, *226*, 111246. [CrossRef]
27. Sayyad, A.S.; Avhad, P.V. Higher-order model for the thermal analysis of laminated composite, sandwich, and functionally graded curved beams. *J. Therm. Stress.* **2022**, *45*, 382–400. [CrossRef]
28. Ghugal, Y.M.; Kulkarni, S.K.; Borate, R.D. Flexural response of cross ply laminated beams subjected to combined thermal and transverse mechanical loads. *Acta Mech.* **2023**, *234*, 3725–3735. [CrossRef]
29. Zhang, Z.; Sun, Y.; Xiang, Z.; Qian, W.; Shao, X. Transient thermoelastic analysis of rectangular plates with time-dependent convection and radiation boundaries. *Buildings* **2023**, *13*, 2174. [CrossRef]

30. Yu, Y.; Deng, W.; Yue, K.; Wu, P. Viscoelastic solutions and investigation for creep behavior of composite pipes under sustained compression. *Buildings* **2022**, *13*, 61. [CrossRef]
31. Qian, H.; Zhou, D.; Liu, W.; Fang, H.; Lu, W. Elasticity solutions of simply supported laminated cylindrical arches subjected to thermo-loads. *Compos. Struct.* **2015**, *131*, 273–281. [CrossRef]
32. Zhang, Z.; Zhou, D.; Lim, Y.M.; Fang, H.; Huo, R. Analytical solutions for multilayered pipes with temperature-dependent properties under non-uniform pressure and thermal load. *Appl. Math. Model.* **2022**, *106*, 369–389. [CrossRef]
33. Zhang, Z.; Zhou, D.; Zhang, J.; Fang, H.; Han, H. Transient analysis of layered beams subjected to steady heat supply and mechanical load. *Steel Compos. Struct.* **2021**, *40*, 87–100. [CrossRef]
34. Ren, Y.; Huo, R.; Zhou, D. Thermo-mechanical buckling analysis of non-uniformly heated rectangular plates with temperature-dependent material properties. *Thin-Walled Struct.* **2023**, *186*, 110653. [CrossRef]
35. Ren, Y.; Huo, R.; Zhou, D. Buckling and post-buckling analysis of restrained non-uniform columns in fire. *Eng. Struct.* **2022**, *272*, 114947. [CrossRef]
36. Asgari, H.; Bateni, M.; Kiani, Y.; Eslami, M.R. Non-linear thermo-elastic and buckling analysis of FGM shallow arches. *Compos. Struct.* **2014**, *109*, 75–85. [CrossRef]
37. Hosseini, S.A.H.; Rahmani, O. Thermomechanical vibration of curved functionally graded nanobeam based on nonlocal elasticity. *J. Therm. Stress.* **2016**, *39*, 1252–1267. [CrossRef]
38. Li, Z.; Zheng, J.; Zhang, Z.; He, H. Nonlinear stability and buckling analysis of composite functionally graded arches subjected to external pressure and temperature loading. *Eng. Struct.* **2019**, *199*, 109606. [CrossRef]
39. Pi, Y.L.; Bradford, M.A. In-plane thermoelastic behaviour and buckling of pin-ended and fixed circular arches. *Eng. Struct.* **2010**, *32*, 250–260. [CrossRef]
40. Khalili, M.M.; Keibolahi, A.; Kiani, Y.; Eslami, M.R. Dynamic snap-through of functionally graded shallow arches under rapid surface heating. *Thin-Walled Struct.* **2022**, *178*, 109541. [CrossRef]
41. Javani, M.; Kiani, Y.; Eslami, M.R. Geometrically nonlinear rapid surface heating of temperature-dependent FGM arches. *Aerosp. Sci. Technol.* **2019**, *90*, 264–274. [CrossRef]
42. Babaei, H.; Kiani, Y.; Eslami, M.R. Large amplitude free vibration analysis of shear deformable FGM shallow arches on nonlinear elastic foundation. *Thin-Walled Struct.* **2019**, *144*, 106237. [CrossRef]
43. Babaei, H.; Kiani, Y.; Eslami, M.R. Geometrically nonlinear analysis of shear deformable FGM shallow pinned arches on nonlinear elastic foundation under mechanical and thermal loads. *Acta Mech.* **2018**, *229*, 3123–3141. [CrossRef]
44. Zhang, P.; Fu, Y. A higher-order beam model for tubes. *Eur. J. Mech. A/Solids.* **2013**, *38*, 12–19. [CrossRef]
45. She, G.L.; Yuan, F.G.; Karami, B.; Ren, Y.R.; Xiao, W.S. On nonlinear bending behavior of FG porous curved nanotubes. *Int. J. Eng. Sci.* **2019**, *135*, 58–74. [CrossRef]
46. Babaei, H.; Kiani, Y.; Eslami, M.R. Geometrically nonlinear analysis of functionally graded shallow curved tubes in thermal environment. *Thin-Walled Struct.* **2018**, *132*, 48–57. [CrossRef]
47. Malekzadeh, P. Two-dimensional in-plane free vibrations of functionally graded circular arches with temperature-dependent properties. *Compos. Struct.* **2009**, *91*, 38–47. [CrossRef]
48. Lim, C.W.; Yang, Q.; Lü, C.F. Two-dimensional elasticity solutions for temperature-dependent in-plane vibration of FGM circular arches. *Compos. Struct.* **2009**, *90*, 323–329. [CrossRef]
49. Xu, Y.; Zhou, D. Two-dimensional thermoelastic analysis of beams with variable thickness subjected to thermo-mechanical loads. *Appl. Math. Model.* **2012**, *36*, 5818–5829. [CrossRef]
50. CEN. *Eurocode 2: Design of Concrete Structures—Part 1–2: General Rules—Structural Fire Design*; European Committee for Standardization (CEN): Brussels, Belgium, 2004.
51. CEN. *Eurocode 3: Design of Steel Structures—Part 1–2: General Rules—Structural Fire Design*; European Committee for Standardization (CEN): Brussels, Belgium, 2005.